Seismic statics application plus trace interpolation

Robert J. Ferguson

ABSTRACT

Simultaneous correction of near-surface statics and trace interpolation is constructed from a Fourier integral representation of wavefield extrapolation and implemented in a least-squares sense. Synthetic examples based on extreme velocity variation and extreme elevation change are used to demonstrate individually and together the aspects of interpolation and of the full statics-application-plus-interpolation (STAPPI). The Husky 2D dataset is used to to demonstrate that this approach interpolates missing traces and applies near-surface statics in a real setting with extreme near surface variation in velocity and elevation.

The method is found to be computationally intensive, and an approximation based on expansion of the Hessian matrix is derived and implemented. A four term implementation of the expansion of the Hessian is developed and tested against the exact operator. The approximate method is found to return comparable data to that of the exact method for all but the most extreme cases. Though computational efficiency is improved by only a scalar relative to the exact algorithm, this work provides an analytic and numerical platform upon which to build an accurate operator that reduces the order associated with computational cost.

INTRODUCTION

Ferguson (2006) presents a method by which severe statics and trace irregularity are corrected. The analytic basis for this method results in an algorithm that is extremely expensive to apply in 2D and impossible to implement in 3D due to cost. An approximation is then developed in Ferguson (2006) by which computational effort is reduced through efficient, limited computation of the Hessian of the corresponding inverse problem. Here, I revisit this approach, and I provide a more solid analytic basis for approximation through series approximation and truncation. Though the resulting algorithm is not significantly more efficient than the algorithm of Ferguson (2006), it represents an analytic form that is useful as a basis for further, and perhaps more fruitful, approximation; and I provide some insight into this in this paper. I develop a more rigorous experimental procedure here as well, with great care taken to illustrate the utility and accuracy of this approach. Further, I introduce a new acronym - STAPPI (statics application plus interpolation) - to the lexicon of geophysics in this paper.

The problem addressed specifically in this paper is that of seismic data recorded in extreme terrains, or in regions of patchy surface access that result in irregular source and receiver spacing. This suffering is the result, partially, of the huge dependence on the fast Fourier-transform in seismic data processing, and the resultant requirement of regular spacing. Then, because irregular spacing makes ambiguous the computation of a spatial Nyquist, maximum phase angle is suspect, and spurious energy propagates through all stages of processing and imaging. Further, irregular trace-spacing introduces a 'footprint' of migration artifacts when data are imaged (Nemeth et al., 1999, provide numerous ex-

amples). Data, therefore, should be *regularized* prior to processing and imaging.

Currently, as a remedy for irregular trace-spacing, filters are used to construct missing traces from the spectra of surrounding traces (Spitz, 1991; Liu and Sacchi, 2004). As well, the interpolation properties of wave propagation can be used to fill empty trace-locations (Ronen, 1987; Zhu and Lines, 1997). In Fourier reconstruction, sparse Fourier inversion is used to estimate missing traces (Duijndam et al., 1999; Zwartjes and Duijndam, 2000).

Besides the problem of irregular trace spacing, conditions that result in irregular data are often associated with strong heterogeneity and/or anisotropy close to the surface. Reflections of interest in the deeper section appear distorted in such areas, and when analyzed for moveout, for example, erroneous velocity-interpretation can result, and imaging is compromised further — beyond problems associated with missing traces. Offshore, rugosity of the seafloor can have a similar effect — in particular when water is shallow (Ferguson and Mosher, 2003).

Numerous approaches exist to correct for complex near-surface. Berryhill (1985) mitigates the effect of heterogeneous surface-layers with wavefield-extrapolation operators based on the wave equation. Berryhill (1979) uses a wave-equation approach to improve the coherence of reflections on synthetic zero-offset data, also on real, prestack-data. Wiggins (1984) provides similar examples using data from a physical model. Yilmaz and Lucas (1986) improve velocity analysis by using a wave-equation based correction for near-surface variation. Bevc (1997), and Shtivelman and Canning (1987) demonstrate the superiority of wave-equation based correction over the more common elevation-statics (restriction of rays to normal incidence). At their core, all of these methods are ray-based implementations (see for example Schneider (1978)), and most use only smoothly varying velocities (presumably due to limitations in raytracing). Reshef (1991) uses a scheme analogous to the Phase-shift-plus-interpolation method (Gazdag and Sguazzero, 1985) to datum wavefields recorded on irregular surfaces.

In Ferguson (2006), the problems of irregular spacing of traces and statics are addressed simultaneously using damped least-squares. Missing traces are replaced with null traces so that the actual and nominal trace spacings are equal, and this produces an even-determined inverse problem. Then, following the example of Kühl and Sacchi (2004), a weighting matrix is introduced so that dead, edited, or padded traces are given zero weight during inversion. A minimum-roughness criterion (Nemeth et al., 1999, reverse VSP example) is then imposed to help ensure uniqueness, and a user parameter ε controls how rough/smooth the result appears. A regularized/datumed wavefield is then computed that minimizes a combination of weighted prediction-error and solution roughness (Ferguson, 2006). To accommodate statics correction, inversion is done in a modified version of the the layer-by-layer approach of Reshef (1991).

Similar to other authors, Ferguson (2006) finds that computation of the Hessian in regularization/datuming is very costly for large numbers of traces. Chavent and Plessix (1999), for example, use efficient, partial mass-lumping to determine the Hessian associated with least-squares Kirchhoff migration. Guitton (2004) approximates the Hessian and corrects Kirchhoff imaging using banks of nonstationary match-filters. Kühl and Sacchi (2004) use

efficient, Fourier-domain operators (Gazdag and Sguazzero, 1984; Margrave and Ferguson, 1999, phase-shift-plus-interpolation, and nonstationary-phase shift respectively) to compute the Hessian associated with least-squares, double-square-root imaging.

In this paper, I begin with the general expression for regularization and redatum by the Newton method developed by Ferguson (2006). I depart from this development at the point of approximation of the Hessian. Where Ferguson (2006) offers a sparse matrix-operator that is fast to compute, I develop an asymptotic approximation that I truncate. My development here provides a prescription for fast calculation of the Hessian plus an analytic framework for further study. In contrast, Ferguson (2006) provides only a prescription for fast calculation plus a qualitative justification. The value in the current work, therefore, lies with the analytic framework, and in the anticipation that an even faster perscription is possible.

In addition to provision of an analytic framework for STAPPI that has potential for wider usage, I test STAPPI rigorously with real and synthetic data. I recognize that, though the interpolation and statics aspects of STAPPI are combined, they may be separated, so I test STAPPI first as an interpolator, and then as a combined interpolator and statics applier. I demonstrate that, for $\Delta z = 0$, STAPPI reduces to an interpolator that is potentially much faster than full STAPPI.

Based on synthetic models and data, I find that, under extreme velocity variation, STAPPI run as an interpolator recovers reliable trace data for moderate and even severe trace decimation, and I find that the approximate operator returns results near identical to the exact operator*.

I then add extreme variation in receiver depth to these models, recompute the data, decimate, and I find that full STAPPI is able again to recover reliable trace data. Here, however, differences between the approximate operator and the exact operator are more apparent - especially in their spectra. Significant differences, however, are restricted to severe decimation. I find that as severity of decimation increases, maximum phase-angle in the data decreases with increased frequency. I identify this relationship as the price paid for irregular trace coverage.

Based on real data, I find that, as an interpolator $(\Delta z = 0)$, STAPPI is quite tolerant of strong velocity contrast and elevation change. I find that decreased phase-angle-with-with-frequency is much less apparent on the real data compared to the synthetic data owing, probably, to the reduced relative aperture of the real and synthetic data. Full STAPPI and its approximation, implemented within the procedure of Reshef (1991), provide effective interpolation and statics correction (based on a velocity model derived by turning-wave tomography).

To test potentially cheap alternatives to STAPPI, I compare these results to statics correction by generalized phase-shift-plus-interpolation (GPSPI) (Gazdag and Sguazzero,

*I define *moderate* decimation as the setting 50% of traces to NULL randomly, and I define *severe* as the setting to NULL 80% of traces randomly.

1984; Margrave and Ferguson, 1999) implemented within the procedure of Reshef (1991). I interpolate the data with approximate STAPPI and then apply statics with GPSPI. I find that considerable spurious-energy is present in the GPSPI output and that the resulting spectrum is disordered. I repeat the experiment with conventional statics, and find, surprisingly, that the GPSPI result is not much better than the statics result. I conclude that, as a cheap alternative to STAPPI, interpolation by approximate STAPPI followed by conventional statics is a good solution for these data when compared to interpolation and GPSPI.

To verify the expectation that GPSPI will interpolate as a natural outcome of statics correction (Berryhill, 1985), I apply GPSPI to the uninterpolated data. Though traces are interpolated, spurious energy very strong, and the spectrum is increased in disorder relative to interpolation followed by GPSPI. I repeat this experiment with conventional statics, and again, surprisingly, the spectrum is as disordered within the non-evanescent region as is the GPSPI spectrum.

THEORY

Given monochromatic wavefield ψ_z, the Newton-method solution (Tarantola, 1987, pg. 251) for extrapolated wavefield $\psi_{z+\Delta z}$ is (Ferguson, 2006)

$$\psi_{z+\Delta z} = \left[U^A_{-\Delta z}\, W_e\, U_{-\Delta z} + \varepsilon^2 W_m\right]^{-1} U^A_{-\Delta z}\, W_e\, \psi_z, \tag{1}$$

where W_e and W_m are a weighting operator and a smoothing operator respectively, and ε^2 is a scalar that controls the amount of smoothing (Menke, 1989, pg. 53 - 54). Operator $U_{-\Delta z}$ and its adjoint $U^A_{-\Delta z}$ are known as one-way operators that move wavefields distance $-\Delta z$ according to a user-defined model of seismic velocity (Margrave and Ferguson, 1999; Ferguson and Margrave, 2002).

Computationally, $U_{-\Delta z}$ and $U^A_{-\Delta z}$ are matrices that can be very large. For 2D data, these matrices may have hundreds or thousands of columns and a similar number of rows. For 3D data, $U_{-\Delta z}$ and $U^A_{-\Delta z}$ are still matrices (Berkhout, 1985), but dimensions scale by hundreds or thousands depending on acquisition design. Without approximation, computation of $\left[U^A_{-\Delta z}\, W_e\, U_{-\Delta z}\, \psi_z\left(x'\right)\right](x)$ within equation 1 is prohibitively expensive in 2D, and impossible (practically speaking) in 3D currently.

Ferguson (2006) and Kühl and Sacchi (2004) explore different, *ad-hoc* approximations to

$$S_{\Delta z} = U^A_{-\Delta z}\, W_e\, U_{-\Delta z}, \tag{2}$$

for use within Hessian of equation 1. Kühl and Sacchi (2004) use phaseshift-plus-interpolation (PSPI) (Gazdag and Sguazzero, 1984) within a conjugate gradient framework, and Ferguson (2006) computes and applies directly only a limited number of diagonals for $S_{\Delta z}$, and then computes the inverse using an efficient LU operator. This approach results in a dip-limited operator related to the $\omega - x$ migration of Berkhout (1985). Moreover, though LU inversion is implemented, a conjugate gradient solution is contemplated by the author currently, and it is expected to speed inversion considerably.

Though the development of Ferguson (2006) results in improvements in computational efficiency, diagonal limiting provides little analytic insight, for example for error analy-

sis, or for development of further improvements, so an analytic approximation to $S_{-\Delta z}$ is desirable. From Ferguson (2006), given arbitrary wavefield ψ_z,

$$[S_{\Delta z}\psi_z(x')](x) = \frac{1}{(2\pi)^4}\int \psi_z(x')\, e^{-i[k_x, y-x']} e^{-i[k'_x, x-y]} \alpha(y, k'_x)_{\Delta z}\, \tilde{\alpha}(y, k_x)_{-\Delta z}\, dk_x\, dy\, dk'_x\, dx', \quad (3)$$

where extrapolator α is

$$\alpha_{\Delta z} = e^{i\Delta z k_z}, \quad (4)$$

and, for temporal frequency $|\omega| = \omega$, wavenumbers k_z are

$$k_z(y, k_x) = \begin{cases} \operatorname{sgn}(\Delta z)\; k(y)\sqrt{1 - \frac{|k_x|^2}{k^2(y)}} & \text{if} \quad \frac{|k_x|^2}{k^2(y)} \le 1; \\ i\operatorname{sgn}(\Delta z)\; k(y)\sqrt{1 - \frac{|k_x|^2}{k^2(y)}} & \text{if} \quad \frac{|k_x|^2}{k^2(y)} > 1, \end{cases} \quad (5)$$

where

$$k(y, \omega) = \frac{\omega}{v(y)}, \quad (6)$$

and v is seismic velocity that varies laterally within the thin slab.

As it is, operator $S_{\Delta z}$ is extremely costly to apply. In 2D, for example, Ferguson (2006) finds that cost is $\propto N^3$ where N is the number of traces. This cost is the cost of the inner loop of the inversion, and outside it is a loop over temporal frequency, and then a loop over depth. For hundreds of traces, frequencies, and depths, inversion of a single trace gather can run for hours on a single processor. In 3D, cost of the inner loop remains $\propto N^3$, however, loops associated with the x-line coordinate are introduced, and cost of the basic-operator increases to N^6 assuming equal numbers of inline and x-line traces. For $N = 1000$, for example, cost is $\propto 10^{18}$ flops per frequency per depth.

APPROXIMATE HESSIAN

Because the Newton method implemented using equation 3 is costly to implement in 3D, some kind of approximation must be considered. Begin with equation 3, and introduce coordinates $\xi = k'_x - k_x$, $k'_x = \xi + k_x$, and $d\xi = dk'_x$ to get

$$[S_{\Delta z}\,\psi(x')](x) = \frac{1}{(2\pi)^4}\int \psi(x')\, e^{iy\xi} e^{ix'k_x} e^{-ix[\xi+k_x]} \alpha_{\Delta z}(y, \xi + k_x)\, \tilde{\alpha}_{-\Delta z}(y, k_x)\; dk_x\, dy\, d\xi\, dx'. \quad (7)$$

Expand $\alpha(\xi + k_x)_{\Delta z}$ as a Taylor series in k_x according to

$$\alpha(\xi + k_x)_{\Delta z} = \sum_{j=0}^{\infty} \frac{1}{j!}\left[\partial^j_{k_x} \alpha(k_x)_{\Delta z}\right] \xi^j, \quad (8)$$

and then compute $y \to \xi$ to eliminate an integral in favour of an infinite sum (that we may expect to truncate later) so that

$$[S_{\Delta z}\,\psi(x')](x) = \sum_{j=0}^{\infty} \frac{1}{j!}\frac{1}{(2\pi)^4}\int \psi(x')\, e^{-ik_x[x-x']} e^{-ix\xi}\, \xi^j\, H(\xi, k_x)_{j,\Delta z}\; dk_x\, d\xi\, dx' \quad (9)$$

where

$$H\left(\xi,k_x\right)_{j,\Delta z}=\int e^{iy\xi}\left[\partial_{k_x}^{j}\alpha\left(y,k_x\right)_{\Delta z}\right]\tilde{\alpha}\left(y,k_x\right)_{-\Delta z}\,dy. \tag{10}$$

Because, for generic function f and its spectrum F, differentiation and integration are related through

$$i^j\,\partial_x^j f\left(x\right)\;\leftrightarrow\;\frac{1}{2\pi}\int\xi^j\,F\left(\xi\right)\,e^{-i\xi\,x}\,d\xi, \tag{11}$$

we may compute $\xi\rightarrow x$ to eliminate another integral

$$\left[S_{\Delta z}\,\psi\left(x'\right)\right]\left(x\right)=\sum_{j=0}^{\infty}\frac{i^j}{j!}\frac{1}{\left(2\pi\right)^2}\int\psi\left(x'\right)e^{-ik_x[x-x']}\left[\partial_x^j\,h_j\left(x,k_x\right)_{\Delta z}\right]\,dk_x\,dx', \tag{12}$$

where

$$h_j\left(x,k_x\right)_{\Delta z}=\left[\partial_{k_x}^{j}\alpha\left(x,k_x\right)_{\Delta z}\right]\tilde{\alpha}\left(x,k_x\right)_{-\Delta z}. \tag{13}$$

Our arrival at equation 12 involves elimination of two integrals (four integrals in 3D), for the cost associated with differential operators and an infinite sum. Compared to an integration operator, a differentiation operator is real-valued, and when the series in j is truncated at $n<<N$, the number of non-zero diagonals is $\propto n$. Unfortunately, only a scalar reduction in computational cost is obtained here relative to equation 3. To reduce the order of proportionality, the remaining integral over k_x in equation 12 must be approximated. This last point is explored with moderate success in Ferguson and Fomel (2006), and a later, more comprehensive analysis of how best to approximate equation 3 is planned for the future. For now, it is important, and sufficient, to analyze equation 12 in its current form.

EXAMPLES

A number of synthetic examples and a real examples are presented here to demonstrate STAPPI. The synthetic models are used to demonstrate specific properties of STAPPI in a controlled way. First, 'do nothing' examples are shown to demonstrate that the exact and approximate STAPPI operators are equivalent when no statics and no interpolation is required. Traces are then removed from the input datasets gradually to demonstrate the interpolation aspects of exact vs. approximate STAPPI. Statics are then introduced to the models, and the process of trace decimation is repeated.

For the real-data experiment, a common-source gather is obtained that is regularly sampled but has significant statics effects. Then, a common-source gather that is poorly sample is obtained, and locations of live traces in this gather are used to flag locations of live traces in the common-source gather as 'live'. The remainder of traces in the common-source gather are then set to zero. The undecimated version of the common-source gather is then used as a 'control', and the decimated version is used as input to STAPPI.

Synthetic example

Finite-difference algorithm `afd_shotrec`[†] from the CREWES library is used to generate synthetic data, and four models are considered here. Two of the models (Figures 1a and b) have constant-depth receivers, and as such, they are designed to test only the interpolation part of STAPPI. Analytically, because there is no depth variation in receiver locations, $\Delta z\,(x) = 0$ in equation 1, and $U^A_{-\Delta z} = I$ and $U_{-\Delta z} = I$, where I is identity, and, for these first two models, equation 1 becomes

$$\psi_{z+0} = \left[W_e\, I + \varepsilon^2 W_m\right]^{-1}\, W_e\, \psi_z \tag{14}$$

- a prescription for interpolation only, and ψ_{z+0} is just the interpolated version of ψ_z.

The remaining models (Figures 2a and b) are identical to the first two (Figures 1a and b), but they have significant variation in receiver depth ($\pm$150m over 10km). These models are used to demonstrate simultaneous interpolation and statics correction.

Interpolation

Velocity variation in Figure 1a represents the velocity cross-section of dipping sediments, and it varies linearly between 2000 m/s on the left side and 3725 m/s on the right side. The model in Figure 1b is the cross-section velocity of 2000 m/s sediment (left side) intruded by 3725 m/s salt (right side). Source/receiver geometry for these models is simple, with 512 receivers spaced 20 m apart and buried at a depth of 2800 m. The source array is buried 200 m below the receiver array at 3000 m, and it consists of a line charge plus 5, evenly-spaced point charges. The line charge generates a seismic feature of low temporal relief that is simple to interpolate, and the expectation is that, even when decimation is extreme, interpolation resolves this feature. The point charges, in contrast, generate crossed diffraction-limbs plus high temporal relief, and they represent the greatest challenge to interpolate. The expectation here is that interpolation of these features fails gradually as decimation increases.

Synthetic data for Figure 1a, and their corresponding 2D spectra, are shown in Figure 3. Temporal frequency ω has range $4 \le \omega \le 36$ Hz, and the evanescent boundary defined by

$$\alpha_{\text{MAX}}\, k_{x,EV} = \omega_{EV}, \tag{15}$$

is annotated in red on the spectrum where $\alpha_{\text{MAX}} = 3725$ m/s.

Figure 3a is the undecimated input. The linear event registers on the left side of this figure at $t \sim 0.1$ s on the left, and at $t \sim 0.05$ s on the right, and the point sources register as diffractions with minimum times that align with the linear event. Coherent arrivals below ~ 0.7 s correspond to numerical artifacts from imperfect control of boundary reflections. It's spectrum (Figure 3d) shows coherent energy within the evanescent region. Figure 3b is the interpolated version of Figure 3a by the exact method (recall, there is no decimation or

[†]This algorithm is based on a five or nine point approximation to the Laplacian operator. Here, the 5-point operator is used for efficiency at the expense of high-frequency.

static shift in this example, so this is a 'do nothing' application of STAPPI), and Figure 3c is the approximate version. The value $E_{RMS} = 1.9282e^{-11}$ is RMS error between the exact and interpolated output - the larger the number, the less reliable is the approximation. Both the exact and approximate versions satisfy the *do no harm* criteria for numerical processes in that diffractions and the linear event are preserved, and their spectra are coherent within the evanescent region; they are identical also (E_{RMS} is very small), and this verifies, at least, the numerical implementation of the approximation.

A filter is applied to the interpolated output to reduce evanescent energy, so the interpolated output differs from the input in the evanescent region.

Data are then decimated randomly from 512 traces to 261 traces (Figure 4a). The linear event is now discontinuous, and diffractions are confused in appearance. The spectrum (Figure 4d) of the decimated input shows incoherence on both sides of the evanescent boundary. Exact interpolation (Figures 4b and e) returns a coherent linear event as expected, and diffractions are *healed*. The spectrum has reliable energy up to $\pm\, 0.6\,\mathrm{mm}^{-1}$ when compared the the spectra in Figure 3. This limit in k_x corresponds to a limit on phase angle according to Figure 6a where maximum phase-angle drops from 90 degrees at 22 Hz to 38 degrees at 36 Hz. Further, coherence of events in the spectrum (Figure 4e), however, decreases with ω as an indication that, though much of the data has been recovered, interpolation robustness is bounded in k_x and ω by irregular trace spacing through an, as yet, unknown process.

Interpolated data returned by approximate STAPPI are nearly identical (E_{RMS} is small) to the data of exact STAPPI. The same phase-angle limit is apparent, and event coherence decreases similarly with ω.

Decimation of the input data is then increased to severe, and the original 512 traces are decimated to 60 traces (Figure 5a). The linear event is severely disrupted, and diffractions are no longer identifiable as such. Further, the spectrum of the decimated data is now quite incoherent (Figure 5d) through the entire $k_x - \omega$ range.

Exact and approximate interpolation (Figures 5b and c) reconstruct the linear event, and both interpolations have constructed identifiable diffractions, though significant discontinuity is present on diffraction limbs. Analysis of the spectra verifies that, though not a perfect reconstruction, fairly coherent-data is produced for $k_x \pm 0.3\mathrm{mm}^{-1}$ to about 15 Hz, and maximum phase-angle drops from 90 degrees as 12 Hz and decreases to 10 degrees at 36 Hz (Figure 6b).

Loss of steep dip, and loss of coherence with increasing ω is apparent also on the salt / sediment example (Figures 7 through 9). The 'do nothing' version of the salt / sediment data (Figure 7) verifies the slight damping of the evanescent region used in interpolation, and it verifies the equivalence of the exact and approximate algorithms (E_{RMS} is small).

Moderate decimation of the input data (Figure 8) is accommodated by both interpolators, and interpolated results are coherent - even at the salt / sediment boundary where one might expect difficulty due to *cycle skipping* for example. Spectra are phase-angle limited

as for the previous model, and coherence decreases with increasing ω.

Severe decimation (Figure 9) is also accommodated by both interpolators, and decreased phase-angle and decreased coherence with increased frequency are again apparent.

Statics and interpolation

Statics are now introduced to the interpolation problem. I repeat the previous experiments on data that correspond to the models in Figures 2a and b. I follow the procedure established for interpolation above, that is, I examine first the 'do nothing' case first for each model, though now 'do nothing' involves correcting for statics, and then I proceed through moderate and severe decimation.

Undecimated data, then, that correspond to the model of Figure 2a are shown in Figure 10a and b (spectrum). The linear event is now a rugose arrival due to irregular receiver-depth, and the spectrum is now disorganized even in the non-evanescent region. In the absence of trace decimation, of course, exact and approximate STAPPI simply apply statics according to

$$\psi_{z+\Delta z} = \left[U^A_{-\Delta z}\, U_{-\Delta z} + \varepsilon^2 W_m\right]^{-1} U^A_{-\Delta z}\, \psi_z, \tag{16}$$

where $W_e = I$. Though no interpolation is done, static shifts are corrected, and the linear event is recovered[‡]. Diffraction limbs appear cut-off, and this is verified through inspection of the corresponding spectra (Figures 10e and f). Data coherence is preserved, however, within the non-evanescent region, and the action of statics correction has simply cut the spectrum to be closer to the evanescent boundary than is apparent in Figures 3e and f.

For moderate decimation (Figure 11), the input spectrum (Figure 11d) is disorganized further relative to Figure 10d, though exact and approximate STAPPI return reconstructed linear events and diffractions (Figures 11b and c). The corresponding spectra (Figure 11e and f) exhibit coherence, maximum phase-angles, and decreased coherence-with-ω that compares favourably to simple interpolation (Figures 10e and f).

For severe decimation (Figure 12), the input spectrum (Figure 12d) is, as expected, disorganized further relative to Figure 11d. Exact and approximate STAPPI return reconstructed linear events with some apparent jitter, and diffractions are reliable within further restricted wavenumbers (Figures 12b, c, e and f). For the first time, significant differences between the exact and approximate STAPPI are apparent, with the approximate method showing a hint of numerical instability on the right hand side of Figure 12c. Instability is manifest in the spectrum of approximate STAPPI (Figure 12f) through increased disorganization of the approximate STAPPI relative to the exact algorithm (Figure 12e).

For the salt / sediment model of Figure 2b, the complexity of the velocity model relative to the linear variation causes significant challenge to STAPPI when statics are significant. Exact STAPPI applied to the undecimated data shown in Figure 13a registers a significant

[‡]For Figures 10 through 15, reference velocity $\alpha_{ref} = 2863$ m/s and datum $z_{dat} = 2960$ m are used to shift STAPPIed data away from $t = 0$.

amplitude anomaly as shown in Figure 13b at 2 km distance, and for all times. This spurious amplitude corresponds to a point charge that is located just on the salt / sediment boundary (Figure 2b), and it underscores the non-unitary nature of extrapolators based on Fourier integrals like equation 1 - the operator is unstable in the presence of extreme variation (Dellinger and Etgen, 1996; Margrave and Ferguson, 1999; Le Rousseau and de Hoop, 2001).

The linear event and diffractions shown in Figures 13b and c are recovered otherwise, and their spectra (Figures 13e and f) are more organized after statics correction. Note, careful experimentation, beyond the present exposition, with damping factor ε in equation 1 will result in a compromise between lateral smoothness and reduction of spurious energy. Unlike the simple interpolation, E_{RMS} between exact and approximate STAPPI is quite large, so effects of approximation, as expected, are larger in the presence of statics.

Under moderate decimation (Figure 14a and d), as shown in Figures 14b and c, exact and approximate STAPPI return a coherent linear-event, diffractions are reconstructed, and spectra are organized within the non-evanescent region (Figures 14e and f). The severity of the spurious amplitude is reduced somewhat. Similar to previous examples, reduction in maximum phase-angle is apparent in the spectra, and coherence decreases with increased frequency.

Severe decimation (Figure 15a and d) exacerbates reduction in maximum phase-angle, and coherence frequency, though the linear event is quite reconstructed with reasonable fidelity. As was seen in approximate STAPPI for the linear model (Figure 12c), instability is registered on the right side for all times.

Foothills dataset

STAPPI is applied here to common-source gather SIN 38 (Figure 16, and repeated in 18a) from the Foothills dataset (Stork, 1994). The gather is used as it is as both input data for STAPPI, and as a control so that the performance of STAPPI is evaluated fairly. As input, this gather is decimated such that live and dead trace locations match those of common receiver gather CRG 625 (Figure 17) from the same dataset. The decimated gather is shown in Figure 18b.

To demonstrate STAPPI, an experimental procedure similar to that of the synthetic procedure is followed. That is, the interpolation aspects of STAPPI are investigated, and the exact and approximate versions are compared. Then, full STAPPI in exact mode an approximate mode are studied. Beyond the procedure for the synthetic data, however, the STAPPI results are compared to more to more conventional approaches like GPSPI and conventional statics correction.

Data and spectrum for common-receiver gather 38 (Figure 16) are shown in Figures 18a and e, and the evanescent boundary (equation 15) associated with $\alpha_{\text{MAX}} = 4600$ m/s annotated in red on the spectrum. Data traces in this common-receiver gather are then set to zero according to locations of zero traces in the common source gather of Figure 17. Thus, a test dataset (Figure 18b and f) plus a control dataset (Figures 18a and e) for comparison

are created.

The results of exact and approximate interpolation (no statics) of the test dataset (Figure 18b) are shown in Figures 18c and g and d and h. Annotated E_{RMS} values correspond to the difference between the interpolated data and the control dataset shown in Figure 18a. As was seen in previous experiments with synthetic data, E_{RMS} values for exact and approximate interpolation are identical. Significant coherence is restored to linear events (Figures 18c and d), and the region beyond the evanescent boundary is cleaned up (Figures 18g and h). Data appear low-frequency compared to the control dataset, but this must be regarded as the trade off between event coherence and event sharpness. Similar to the synthetic experiments presented previously, a phaseshift evanescent filter is applied after interpolation, and a significant portion of Rayleigh waves in the control dataset are not restored in the interpolated data.

Tests of full STAPPI are shown in Figure 19. Here, based on the velocity model shown in Figure 20, full STAPPI applied to the undecimated data of Figure 18a is used as the control dataset, and E_{RMS} are referenced to the control[§]. This control dataset for full STAPPI is shown in Figure 19a. Compared with the Figure 18a, significant statics-correction is apparent[¶], and significant Rayleigh-wave energy is removed. Exact STAPPI applied to the test dataset (Figure 18b) is shown in Figure 19b. Compared to the control (Figure 19a), and consistent with results obtained previously with synthetic data, maximum phase-angle (Figure 18f) is reduced, and coherence decreases with increased ω. Similar results are obtained from approximate STAPPI (Figures 18c and g) and, interestingly, E_{RMS} is reduced for approximate STAPPI relative to the exact implementation.

For comparison, approximate STAPPI is applied to the interpolation-only result shown in Figure 18d. That is, approximate STAPPI interpolation is done first followed by approximate STAPPI-statics (equation 16), and the result is shown in Figure 19d. Error E_{RMS} is increased relative the (full) approximate STAPPI (Figure 19c), though maximum phase-angle shows an apparent increase below 30 Hz. Above 30 Hz, the spectrum loses coherence at a greater apparent rate.

Further comparative data are shown in Figure 21. In Figure 21a, GPSPI statics are applied to data interpolated by exact STAPPI (Figure 18c) according to

$$\psi_{z+\Delta z} = U^A_{-\Delta z}\,\psi_{z,I}, \tag{17}$$

where $\psi_{z,I}$ is the interpolated output from exact STAPPI, and where, effectively, when compared to equation 1, no accommodation for missing traces is made in equation 17 so that $(W_e = I)$, $U^A_{-\Delta z}U_{-\Delta z} = I$ is assumed, and $\varepsilon = 0$. In Figure 21a, though E_{RMS} is not significantly higher than for exact STAPPI, serious, low frequency noise is apparent, particularly, between 2 km and 4 km, and between 0 s and 1.5 s, and reflections in this region are obscured relative to the result of exact and approximate STAPPI (Figures 19b and c). Further, spurious diffractions are apparent above the first arrivals. Clearly, the cost

[§]Direct comparison between STAPPI corrected data and the undecimated input is, of course, complicated by events that no longer line up in t.

[¶]We have applied receiver statics only, so source statics will remove statics that remain.

savings associated with exact interpolation of data followed by GPSPI statics rather than the use of approximate STAPPI (Figure 19c) are overcome by inaccuracy.

Conventional statics are applied to the data shown in Figure 19b according to

$$\psi_{z+\Delta z} = \text{Diag}\left(U^A_{-\Delta z}\right)\ \psi_{z,I}, \tag{18}$$

where Diag extracts the diagonal of the GPSPI operator. The result is a a space-domain operator that is non-zero only on the diagonal and corresponds to normal-incidence propagation only. This statics result shown in Figures 21b and f compare favourable to the GPSPI result (Figure 19a and e), and it is, perhaps, superior owing to a reduced presence of spurious diffraction above the first arrivals.

GPSPI is then applied to the raw input (Figure 18b, no interpolation) and the result is shown in Figure 19c and g. Some rudimentary interpolation is apparent in this Figure, and significant Rayleigh-wave energy is removed. The spectrum, when compared to the reference, is quite incoherent within the non-evanescent region. Significant, spurious diffraction-energy is apparent everywhere associated with discontinuous data - the first arrivals for example, and live traces that bound null traces. Similarly, conventional statics is applied to the raw input, and the result is shown in Figure 19d and h. The spectrum, of course, when compared to the reference, has no Rayleigh-wave reduction, as no evanescent boundary is enforced. Note that within the non-evanescent region, the statics spectrum is mostly similar to the GPSPI spectrum (Figure 21c).

That E_{RMS} for the experiments shown in Figure 21 are quite similar casts doubt on the usefulness of E_{RMS} as a measure of error and, perhaps, another measure must be considered.

CONCLUSIONS

From the general expression for regularization and redatum by the Newton method of Ferguson (2006), I have developed an asymptotic approximation that I truncate. The result is a prescription for fast calculation of the required Hessian plus an analytic framework. Though the result is not significantly more efficient than the algorithm of Ferguson (2006), the analytic framework provided here is important for the continued search for efficiencies.

Based on rigorous testing of real and synthetic data, I find that with statics correction turned off, STAPPI is an effective and efficient interpolator. Further, under extreme velocity variation, STAPPI run as an interpolator recovers reliable trace data for moderate and even severe trace decimation, and the approximate operator provides as good a result as the exact operator.

With extreme variation in receiver depth added in, STAPPI recovers reliable trace data, however, it is apparent that the interpolated/statics-corrected STAPPI approximation and exact STAPPI diverge when trace decimation is severe. In terms of error, I find that, as severity of decimation increases, maximum phase-angle in the data decreases with increased frequency.

Using real data, STAPPI as an interpolator is shown to tolerate strong velocity contrast

and elevation change, and decreased phase-angle-with-with-frequency is found to be much less apparent compared to the synthetic data. Full STAPPI and its approximation, implemented within the procedure of Reshef (1991), provide effective interpolation and statics correction (based on a velocity model derived by turning-wave tomography).

Potentially cheap alternatives to STAPPI are tested. First, approximate STAPPI is used to interpolate the real data, and this is followed by generalized-phase-shift-plus-interpolation (GPSPI) implemented within the procedure of Reshef (1991). Spurious-energy is found in the GPSPI output and the resulting spectrum is disordered relative to exact and approximate STAPPI. Conventional statics are applied to the same data and the result is found to be equivalent in quality to the GPSPI. A similar result is found when GPSPI and conventional statics are compared on the uninterpolated data.

REFERENCES

Berkhout, A. J., 1985, Seismic Migration. Imaging of acoustic energy by wavefield extrapolation. A. Theoretical aspects: Elsevier.

Berryhill, J. R., 1979, Wave equation datuming: Geophysics, **44**, No. 08, 1329–1344.

Berryhill, J. R., 1985, Wave equation datuming, *in* Gardner, G. H. F., Ed., Migration of seismic data, Soc. of Expl. Geophys., 331–346, reprinted from Geophysics, 44, 1329-1344.

Bevc, D., 1997, Flooding the topography: Wave-equation datuming of land data with rugged acquisition topography: Geophysics, **62**, No. 05, 1558–1569.

Chavent, G., and Plessix, R. E., 1999, An optimal true-amplitude least-squares prestack depth-migration operator: Geophysics, **64**, No. 2, 508–515.

Dellinger, J., and Etgen, J., 1996, Eigenvalues, singular values, and stability analysis, *in* 66th Ann. Internat. Mtg, Soc. of Expl. Geophys., 1975–1978.

Duijndam, A. J. W., Schonewille, M. A., and Hindriks, C. O. H., 1999, Reconstruction of band-limited signals, irregularly sampled along one spatial direction: Geophysics, **64**, No. 2, 524–538.

Ferguson, R., and Margrave, G. F., 2002, Prestack depth migration by symmetric nonstationary phase shift: Geophysics, **67**, No. 2, 594–603.

Ferguson, R. J., 2006, Regularization and datuming of seismic data by weighted, damped least-squares: Geophysics, **71**, No. 5, U67 – U76.

Ferguson, R. J., and Fomel, S. B., 2006, Interpolation and extrapolation of seismic data using Newton's method: in Mathematical modelling of wave phenomena: AIP Conference Proceedings.

Ferguson, R. J., and Mosher, C., 2003, Fourier integral operators, phase-screens, and their relationship to statics correction: an example from offshore norway, *in* 73rd Annual International Meeting, Society of Exploration Geophysicists, 1881–1884.

Gazdag, J., and Sguazzero, P., 1984, Migration of seismic data by phase-shift plus interpolation: Geophysics, **49**, No. 02, 124–131.

Gazdag, J., and Sguazzero, P., 1985, Migration of seismic data by phase shift plus interpolation, *in* Gardner, G. H. F., Ed., Migration of seismic data, Soc. of Expl. Geophys., 323–330, reprinted from Geophysics, 49, 124-131.

Guitton, A., 2004, Amplitude and kinematic corrections of migrated images for nonunitary imaging operators: Geophysics, **69**, No. 4, 1017–1024.

Kühl, H., and Sacchi, M. D., 2004, Least-squares wave-equation migration for avp/ava inversion: Geophysics, **69**, No. 1, 262–273.

Le Rousseau, J. H., and de Hoop, M. V., 2001, Modeling and imaging with the scalar generalized-screen algorithms in isotropic media: Geophysics, **66**, No. 5, 1551–1568.

Liu, B., and Sacchi, M. D., 2004, Minimum weighted norm interpolation of seismic records: Geophysics, **69**, No. 1, 1560–1568.

Margrave, G. F., and Ferguson, R. J., 1999, Wavefield extrapolation by nonstationary phase shift: Geophysics, **64**, No. 4, 1067–1078.

Menke, W., 1989, Geophysical data analysis: Discrete inverse theory: Academic Press.

Nemeth, T., Wu, C., and Schuster, G. T., 1999, Least-squares migration of incomplete reflection data: Geophysics, **64**, No. 1, 208–221.

Reshef, M., 1991, Depth migration from irregular surfaces with depth extrapolation methods (short note): Geophysics, **56**, No. 01, 119–122.

Ronen, J., 1987, Wave equation trace interpolation: Geophysics, **52**, No. 07, 973–984.

Schneider, W. A., 1978, Integral formulation for migration in two-dimensions and three-dimensions: Geophysics, **43**, No. 01, 49–76.

Shtivelman, V., and Canning, A., 1987, Datum correction by wave equation extrapolation, *in* 57th Ann. Internat. Mtg, Soc. of Expl. Geophys., Session:S3.2.

Spitz, S., 1991, Seismic trace interpolation in the F-X domain: Geophysics, **56**, No. 06, 785–794.

Stork, C., 1994, Demonstration of MVA tomography with controls and constraints for determining an accurate velocity model for prestack depth migration, *in* 64th Ann. Internat. Mtg, Soc. of Expl. Geophys., 1338–1342.

Tarantola, A., 1987, Inverse problem theory: Elsevier Science.

Wiggins, J. W., 1984, Kirchhoff integral extrapolation and migration of nonplanar data: Geophysics, **49**, No. 08, 1239–1248.

Yilmaz, O., and Lucas, D., 1986, Prestack layer replacement: Geophysics, **51**, No. 07, 1355–1369.

Zhu, J., and Lines, L. R., 1997, Implicit interpolation in reverse-time migration: Geophysics, **62**, No. 03, 906–917.

Zwartjes, P., and Duijndam, A., 2000, Optimizing reconstruction for sparse spatial sampling, *in* 70th Ann. Internat. Mtg, Soc. of Expl. Geophys., 2162–2165.

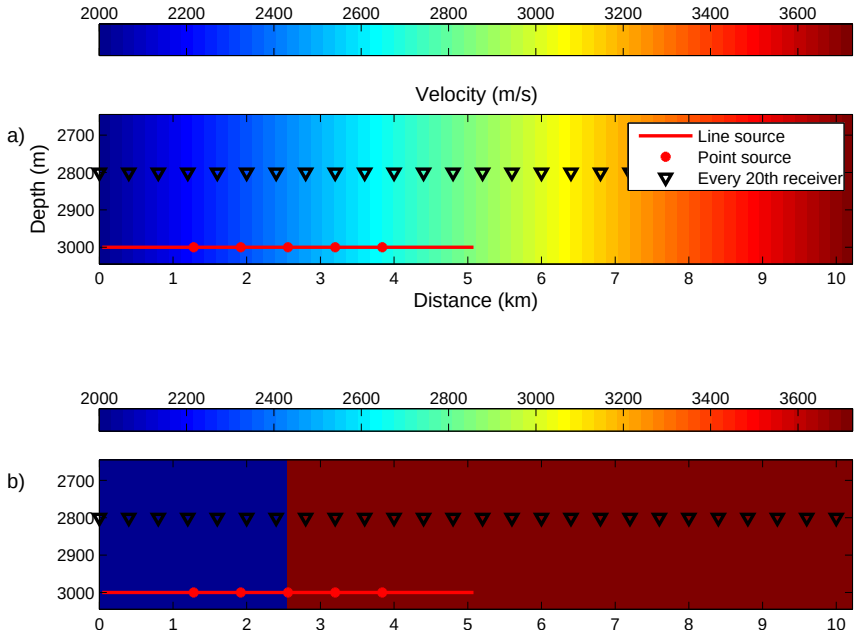

FIG. 1. Velocity models with source/receiver geometry annotated. For visual clarity, every 20th receiver is annotated - the actual trace spacing is 20m. a) Linear velocity variation. b) A step-function velocity.

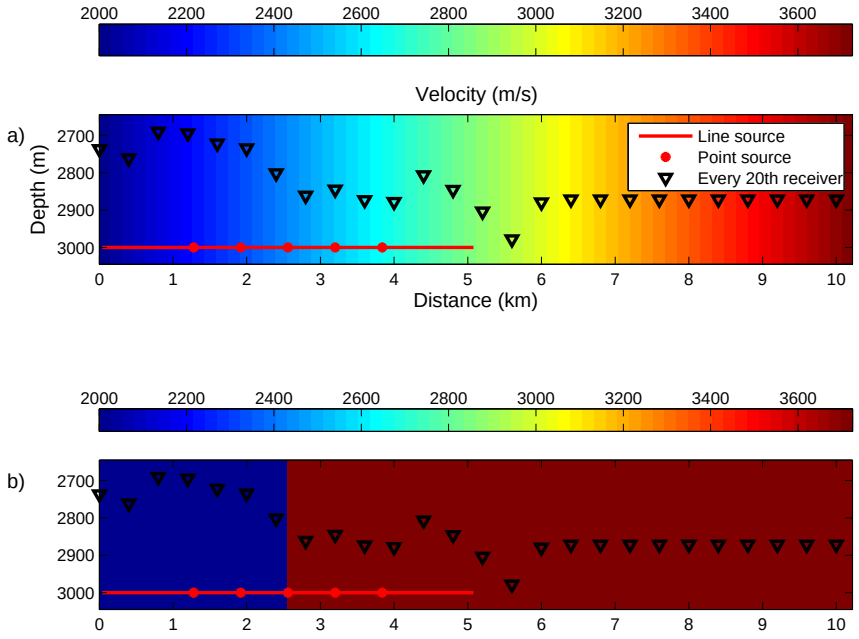

FIG. 2. Velocity models with source/receiver geometry annotated. a) Linear velocity variation. b) A step-function velocity.

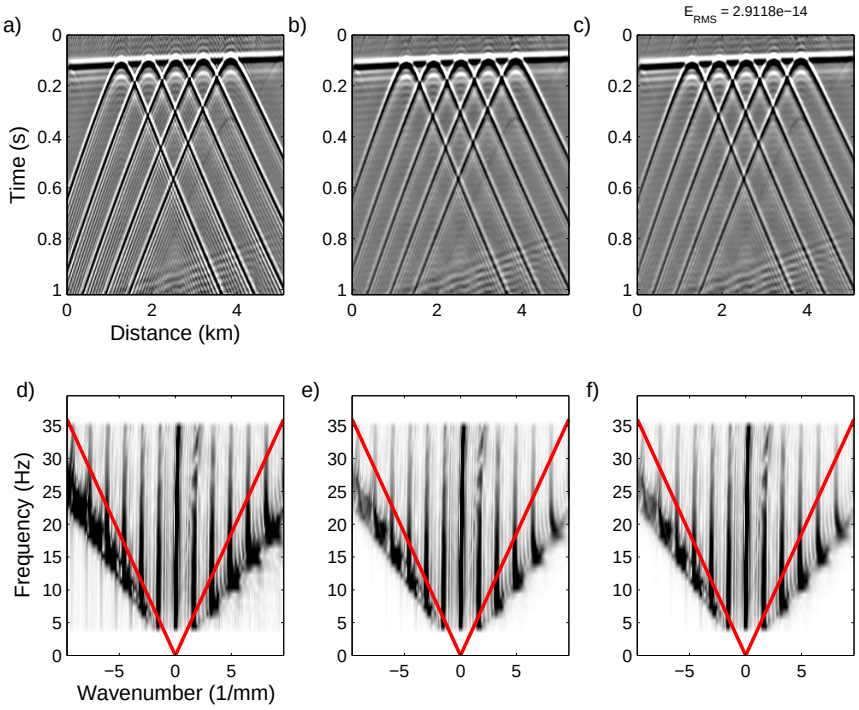

FIG. 3. Control experiment (no decimation) for the source/receiver geometry of Figure 1a. a) Input data with no trace decimation. b) Exact interpolation. c) Asymptotic interpolation. d) Spectrum of a. e) Spectrum of b. f) Spectrum of c. The evanescent boundary is indicated by the red line.

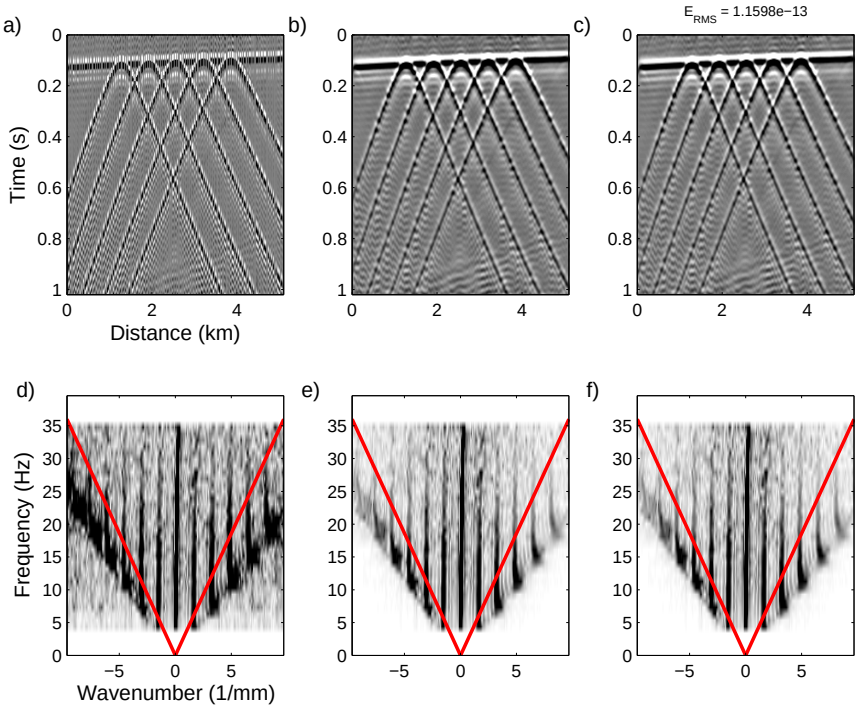

FIG. 4. Interpolation experiment for the source/receiver geometry of Figure 1a and moderate trace-decimation. (based on Figure 1a). a) Input data are decimated randomly from 512 traces to 261 traces. b) Exact interpolation. c) Asymptotic interpolation. d) Spectrum of a. e) Spectrum of b. f) Spectrum of c. The evanescent boundary is indicated by the red line.

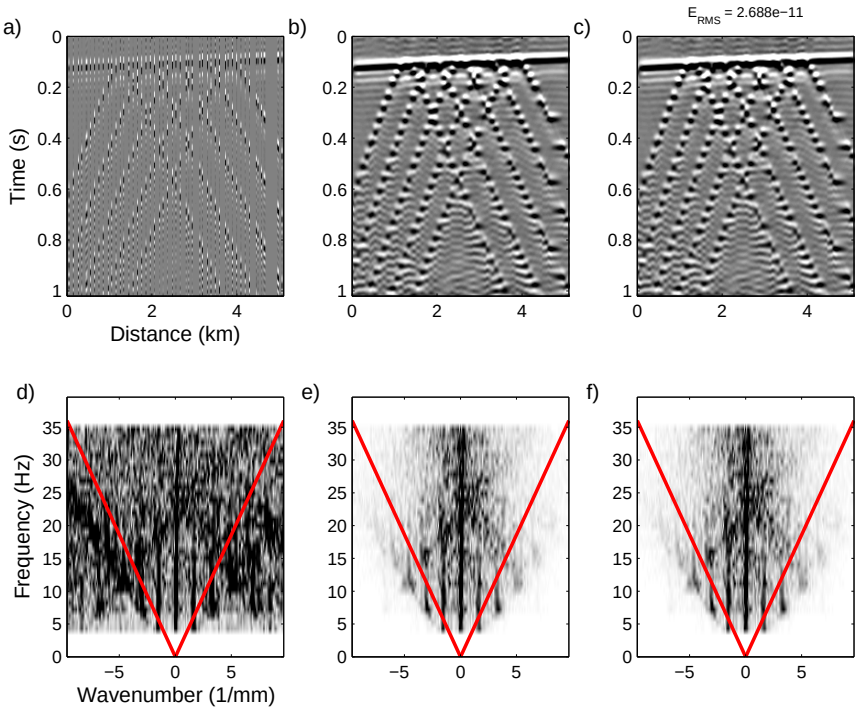

FIG. 5. Interpolation experiment for the source/receiver geometry of Figure 1a and severe trace-decimation. (based on Figure 1a). a) Input data decimated randomly from 512 traces to 60 traces. b) Exact interpolation. c) Asymptotic interpolation. d) Spectrum of a. e) Spectrum of b. f) Spectrum of c. The evanescent boundary is indicated by the red line.

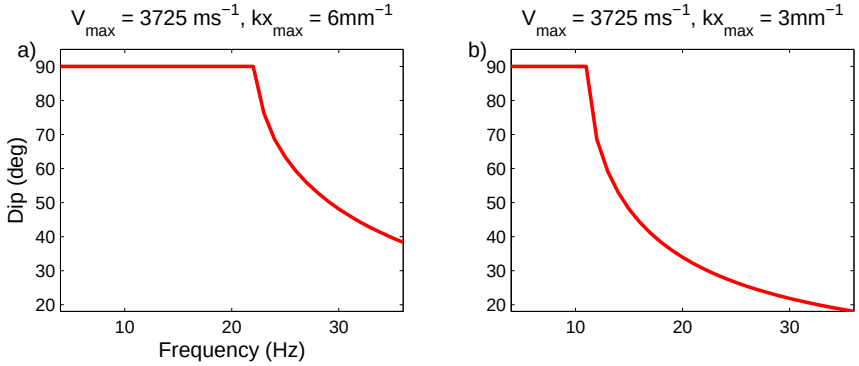

FIG. 6. Maximum phase-andlge vs. frequency for fixed wavenumbers. a) Maximum phase-angle when $-6 \leq k_x \leq 6\,\mathrm{mm}^{-1}$. b) Maximum phase-angle when $-3 \leq k_x \leq 3\,\mathrm{mm}^{-1}$.

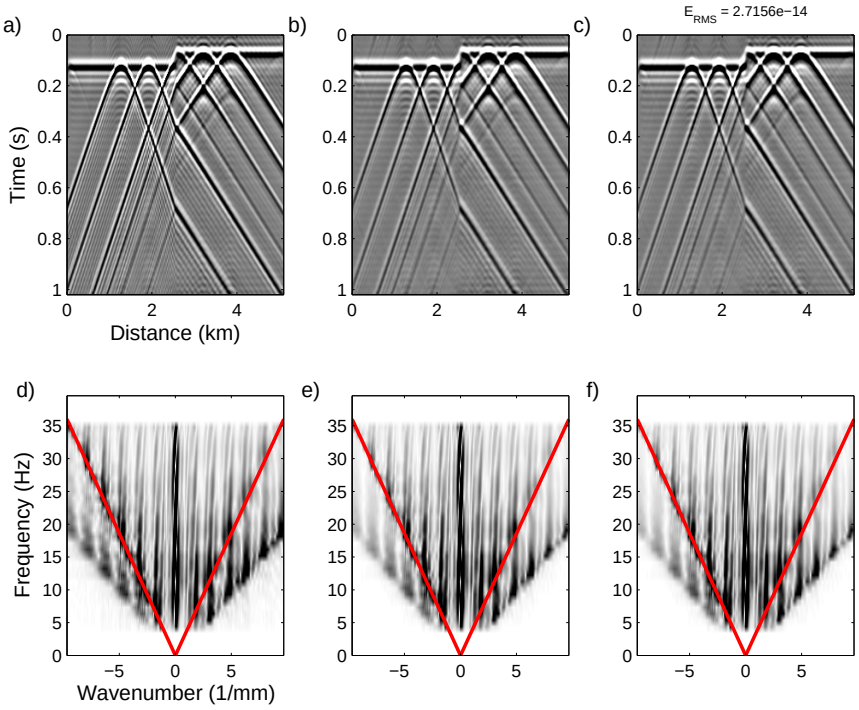

FIG. 7. Control experiment (no decimation) for the source/receiver geometry of Figure 1b. a) Input data with no trace decimation. b) Exact interpolation. c) Asymptotic interpolation. d) Spectrum of a. e) Spectrum of b. f) Spectrum of c. The evanescent boundary is indicated by the red line.

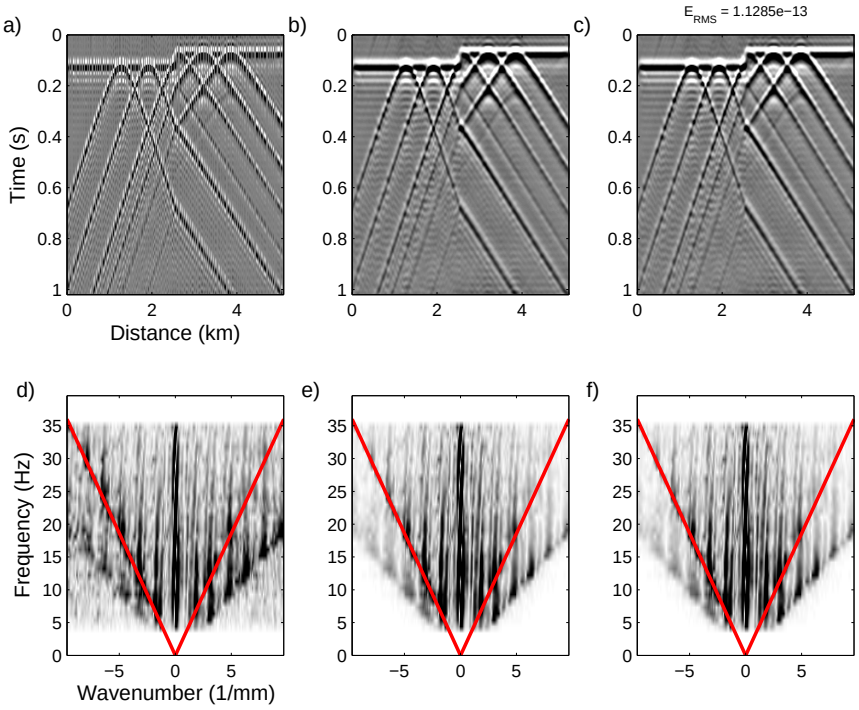

FIG. 8. Interpolation experiment for the source/receiver geometry of Figure 1b and moderate trace-decimation. (based on Figure 1b). a) Input data are decimated randomly from 512 traces to 261 traces. b) Exact interpolation. c) Asymptotic interpolation. d) Spectrum of a. e) Spectrum of b. f) Spectrum of c. The evanescent boundary is indicated by the red line.

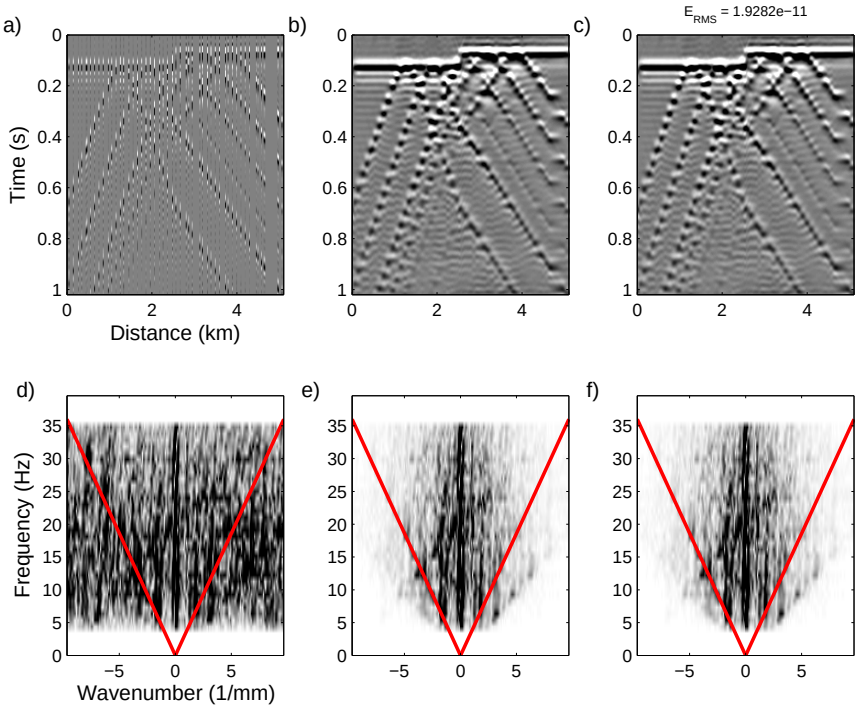

FIG. 9. Interpolation experiment for the source/receiver geometry of Figure 1b and severe trace-decimation. (based on Figure 1b). a) Input data decimated randomly from 512 traces to 60 traces. b) Exact interpolation. c) Asymptotic interpolation. d) Spectrum of a. e) Spectrum of b. f) Spectrum of c. The evanescent boundary is indicated by the red line.

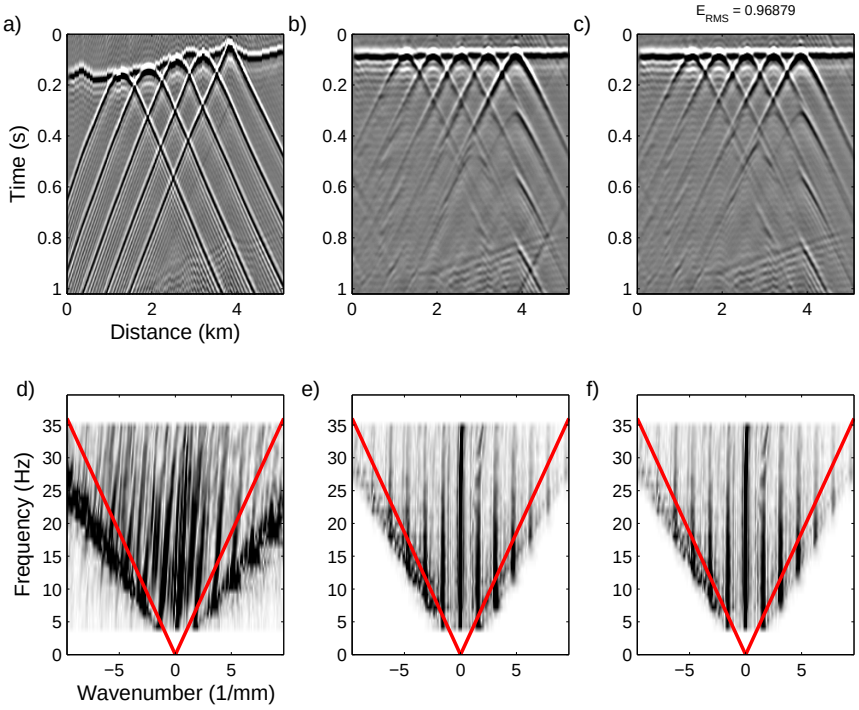

FIG. 10. Control experiment (no decimation) for the source/receiver geometry of Figure 2a. a) Input data with no trace decimation. b) Exact STAPPI. c) Asymptotic STAPPI. d) Spectrum of a. e) Spectrum of b. f) Spectrum of c. The evanescent boundary is indicated by the red line.

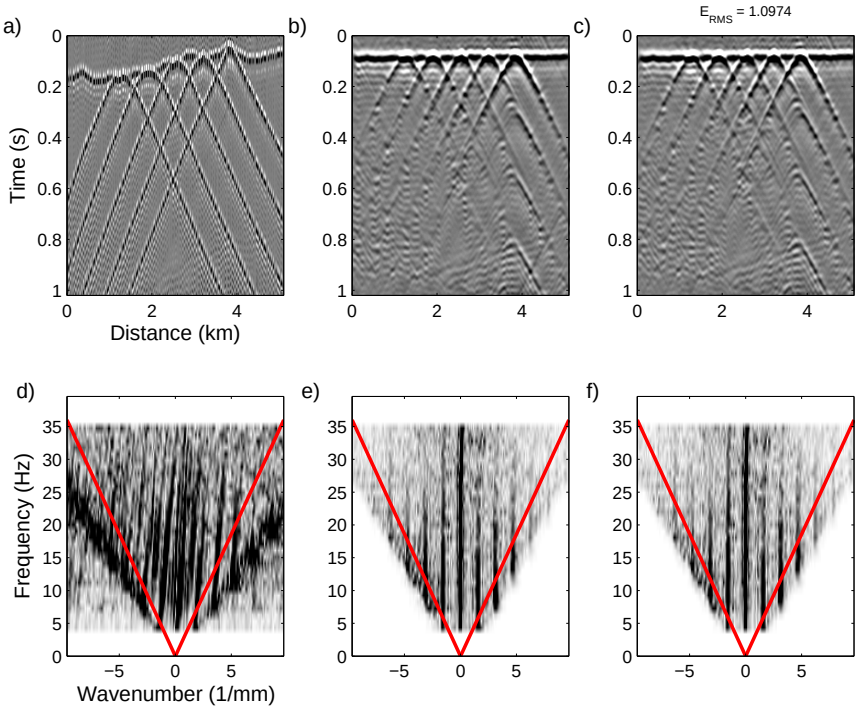

FIG. 11. STAPPI experiment for the source/receiver geometry of Figure 2a and moderate trace-decimation. (based on Figure 2a). a) Input data are decimated randomly from 512 traces to 261 traces. b) Exact STAPPI. c) Asymptotic STAPPI. d) Spectrum of a. e) Spectrum of b. f) Spectrum of c. The evanescent boundary is indicated by the red line.

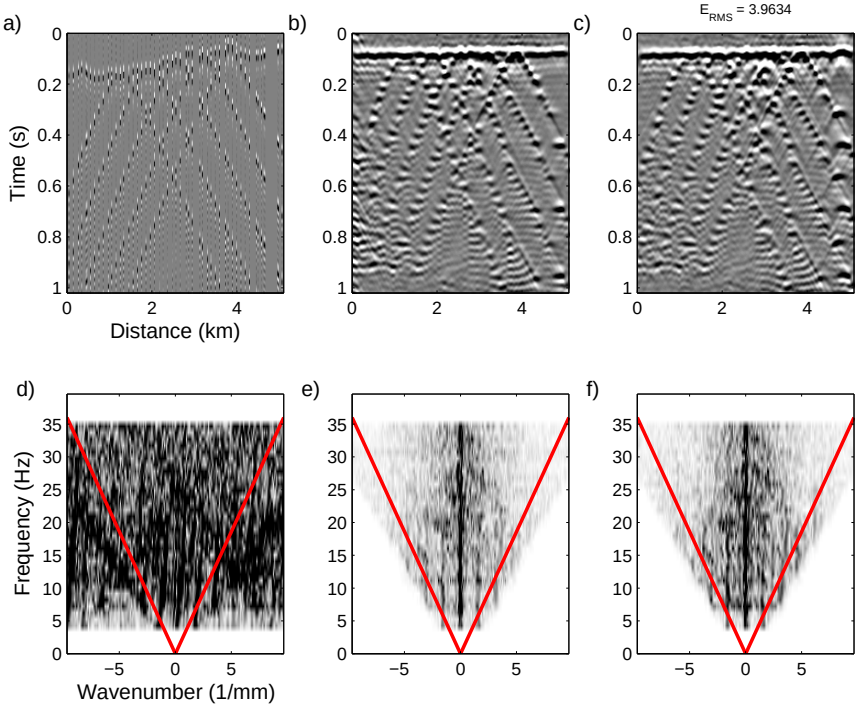

FIG. 12. STAPPI experiment for the source/receiver geometry of Figure 2a and severe trace-decimation. (based on Figure 2a). a) Input data decimated randomly from 512 traces to 60 traces. b) Exact STAPPI. c) Asymptotic STAPPI. d) Spectrum of a. e) Spectrum of b. f) Spectrum of c. The evanescent boundary is indicated by the red line.

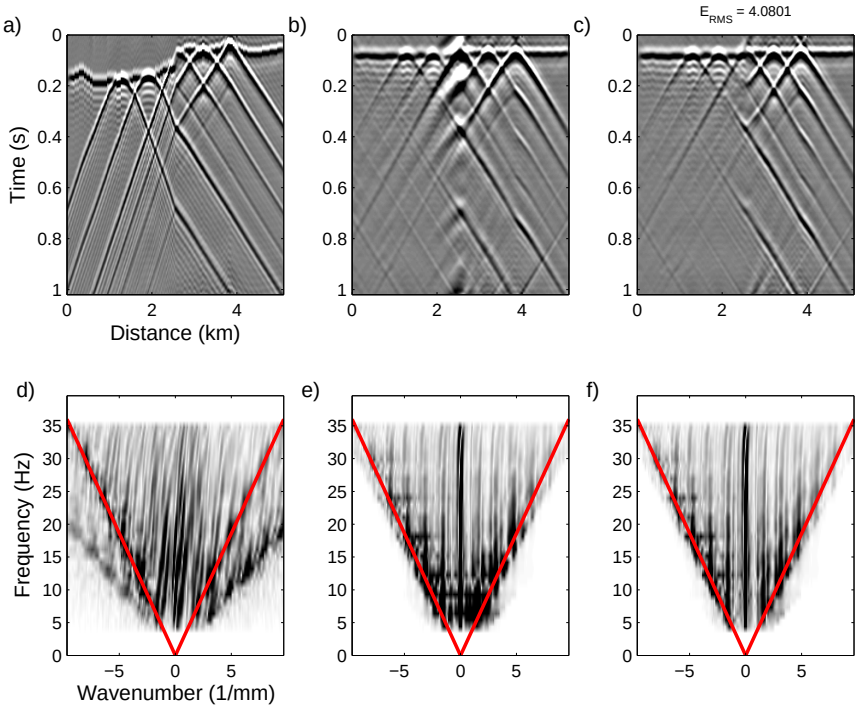

FIG. 13. Control experiment (no decimation) for the source/receiver geometry of Figure 2b. a) Input data with no trace decimation. b) Exact STAPPI. c) Asymptotic STAPPI. d) Spectrum of a. e) Spectrum of b. f) Spectrum of c. The evanescent boundary is indicated by the red line.

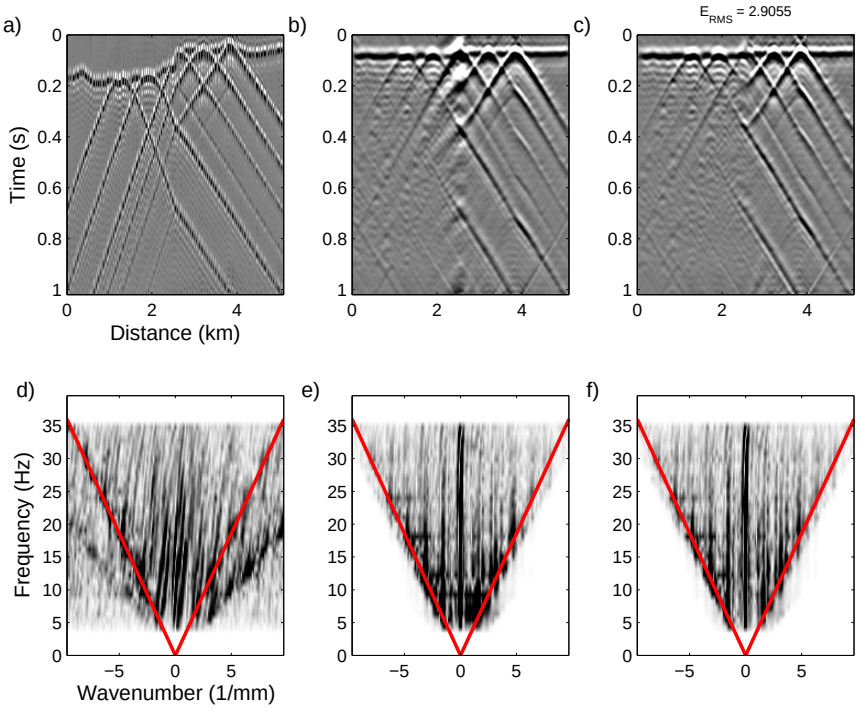

FIG. 14. STAPPI experiment for the source/receiver geometry of Figure 2b and moderate trace-decimation. (based on Figure 2b). a) Input data are decimated randomly from 512 traces to 261 traces. b) Exact STAPPI. c) Asymptotic STAPPI. d) Spectrum of a. e) Spectrum of b. f) Spectrum of c. The evanescent boundary is indicated by the red line.

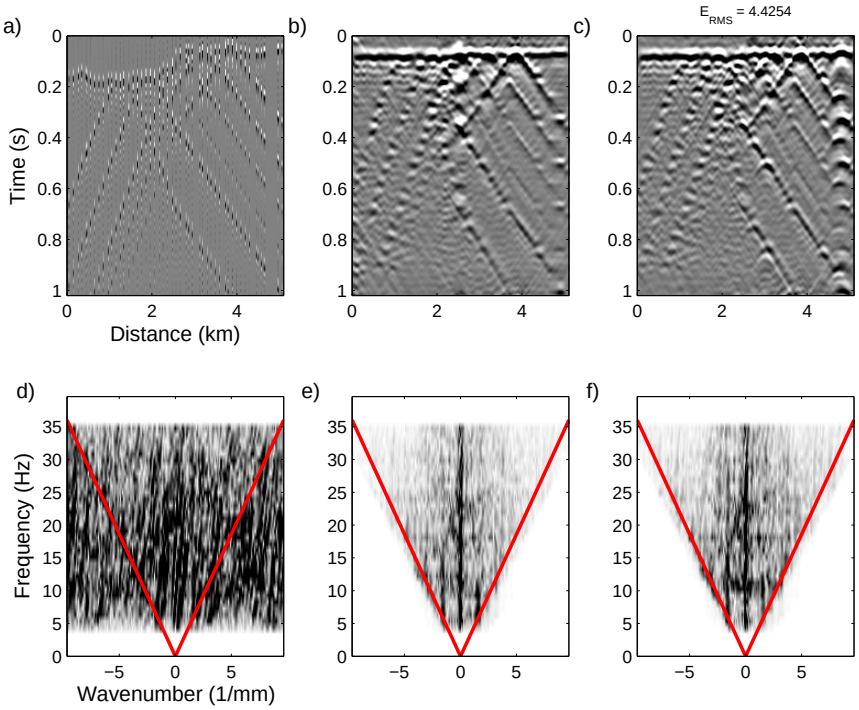

FIG. 15. STAPPI experiment for the source/receiver geometry of Figure 2b and severe trace-decimation. (based on Figure 2b). a) Input data decimated randomly from 512 traces to 60 traces. b) Exact STAPPI. c) Asymptotic STAPPI. d) Spectrum of a. e) Spectrum of b. f) Spectrum of c. The evanescent boundary is indicated by the red line.

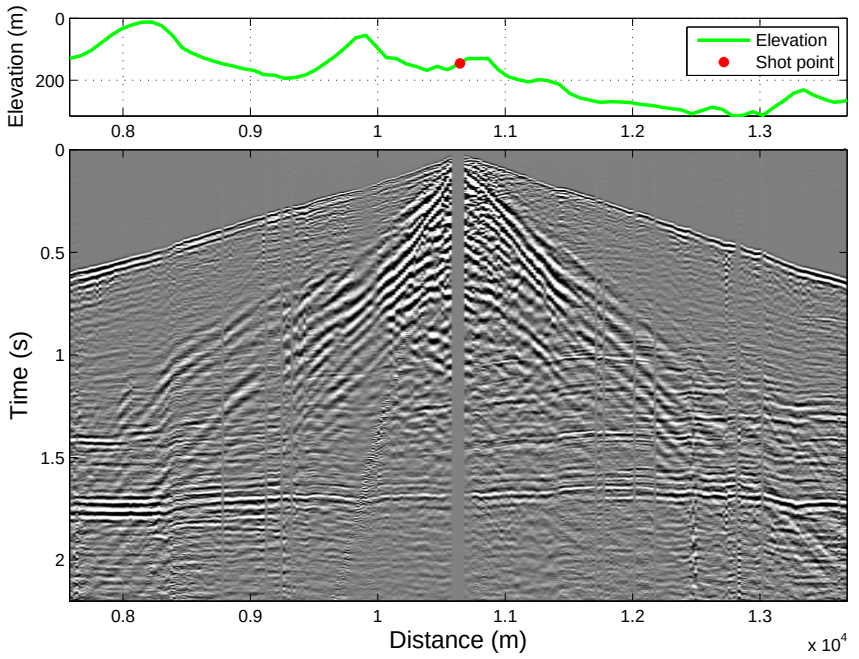

FIG. 16. Common-source gather `SIN_38` from the foothills dataset (Stork, 1994) with elevation profile and source location indicated. With the exception of the receiver gap around the source location, trace spacing is 20 m.

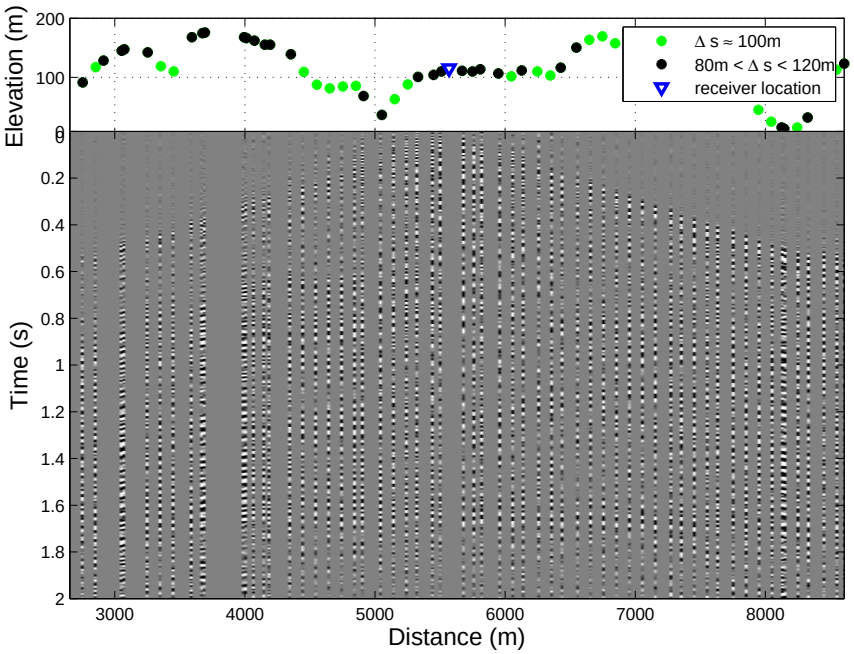

FIG. 17. Common-receiver gather CRG_625 from the foothills dataset (Stork, 1994). Nominal source-spacing is 100 m. Due to extremes in surface conditions, the actual source-spacing varies by $\pm$ 60 m as indicated by black dots.

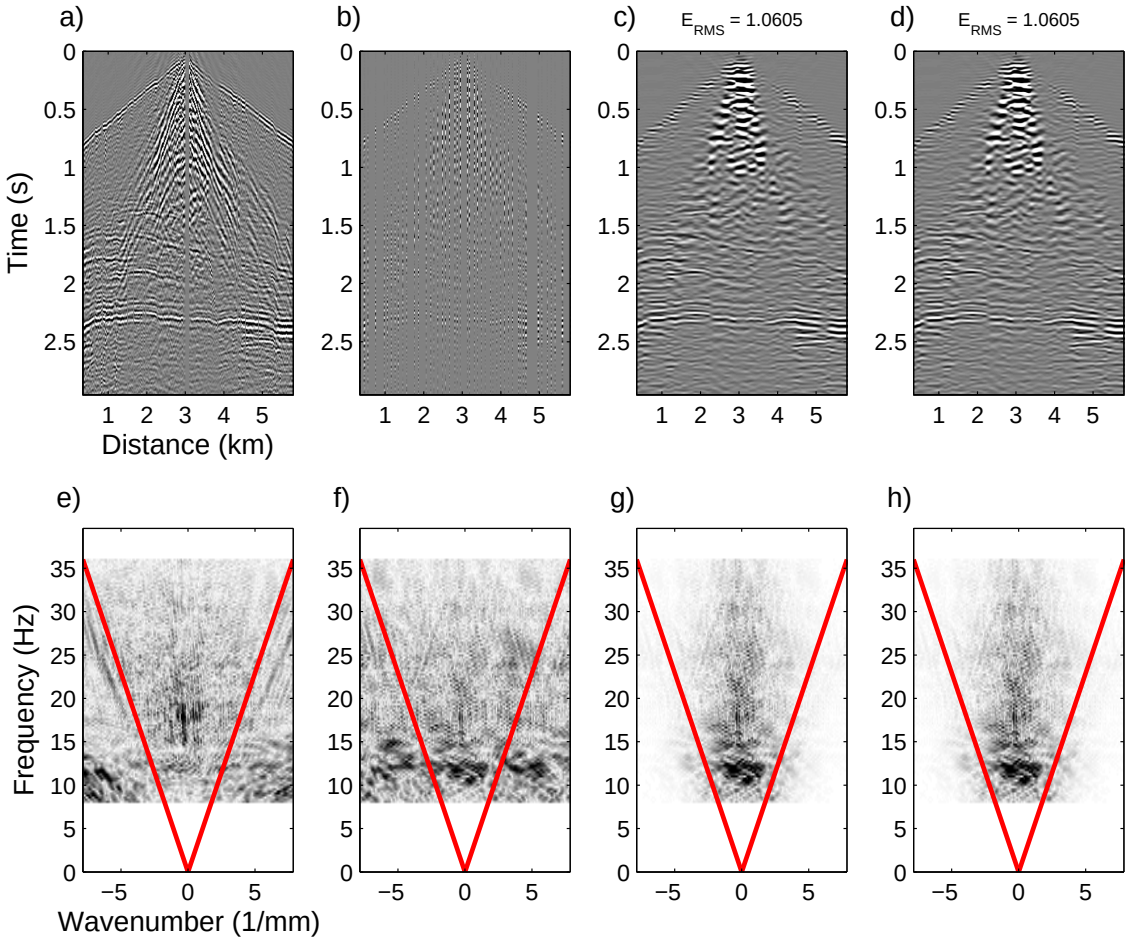

FIG. 18. Interpolation experiments for the foothills dataset. a) Input. b) Decimated input. c) Exact interpolation of b). d) Asymptotic interpolation of b). e) Spectrum of a). f) Spectrum of b). g) Spectrum of c). h) Spectrum of d). The evanescent boundary is indicated by red lines.

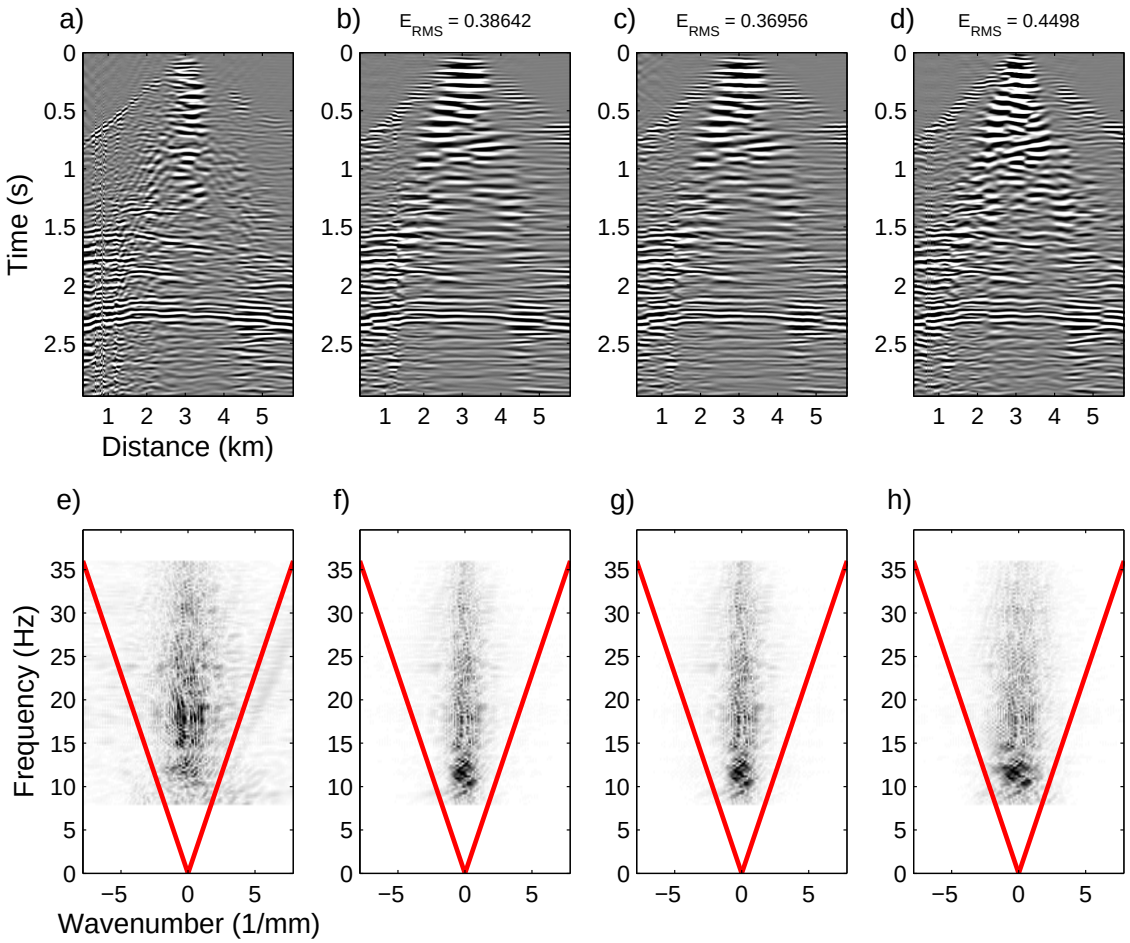

FIG. 19. STAPPI experiments for the data shown in Figure 18a. a) Exact STAPPI applied to the data shown in Figure 18a. b) Exact STAPPI applied to the data shown in Figure 18b. c) Asymptotic STAPPI applied to Figure 18b. d) Asymptotic STAPPI applied to Figure 18d. e) Spectrum of a. f) Spectrum of b. g) Spectrum of c. h) Spectrum of d. The evanescent boundary is indicated by red lines.

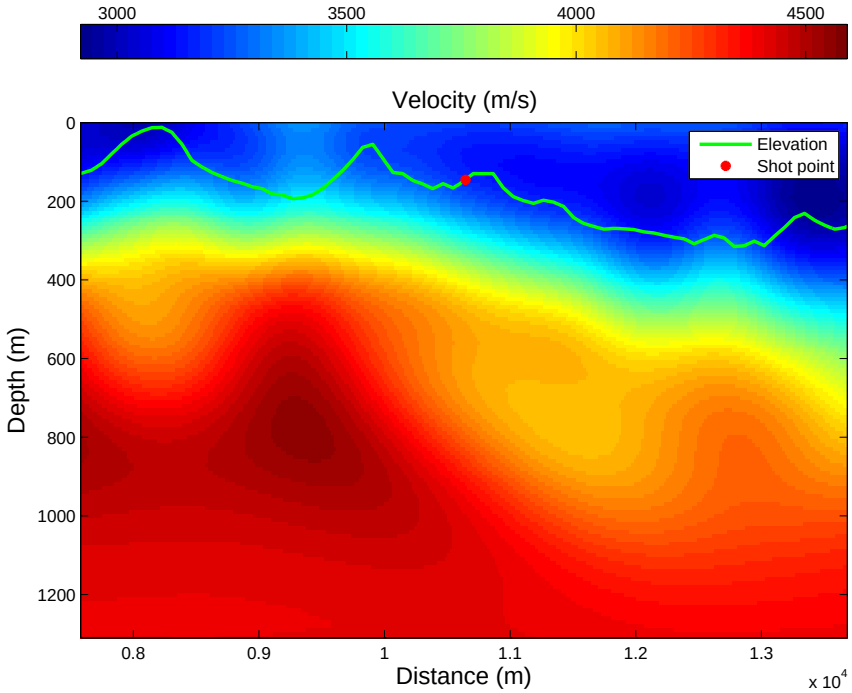

FIG. 20. Part of a velocity model obtained from the foothills dataset (Stork, 1994) by turning wave tomography. The distance range of this model corresponds to the distance range of `SIN_38` (Figure 16).

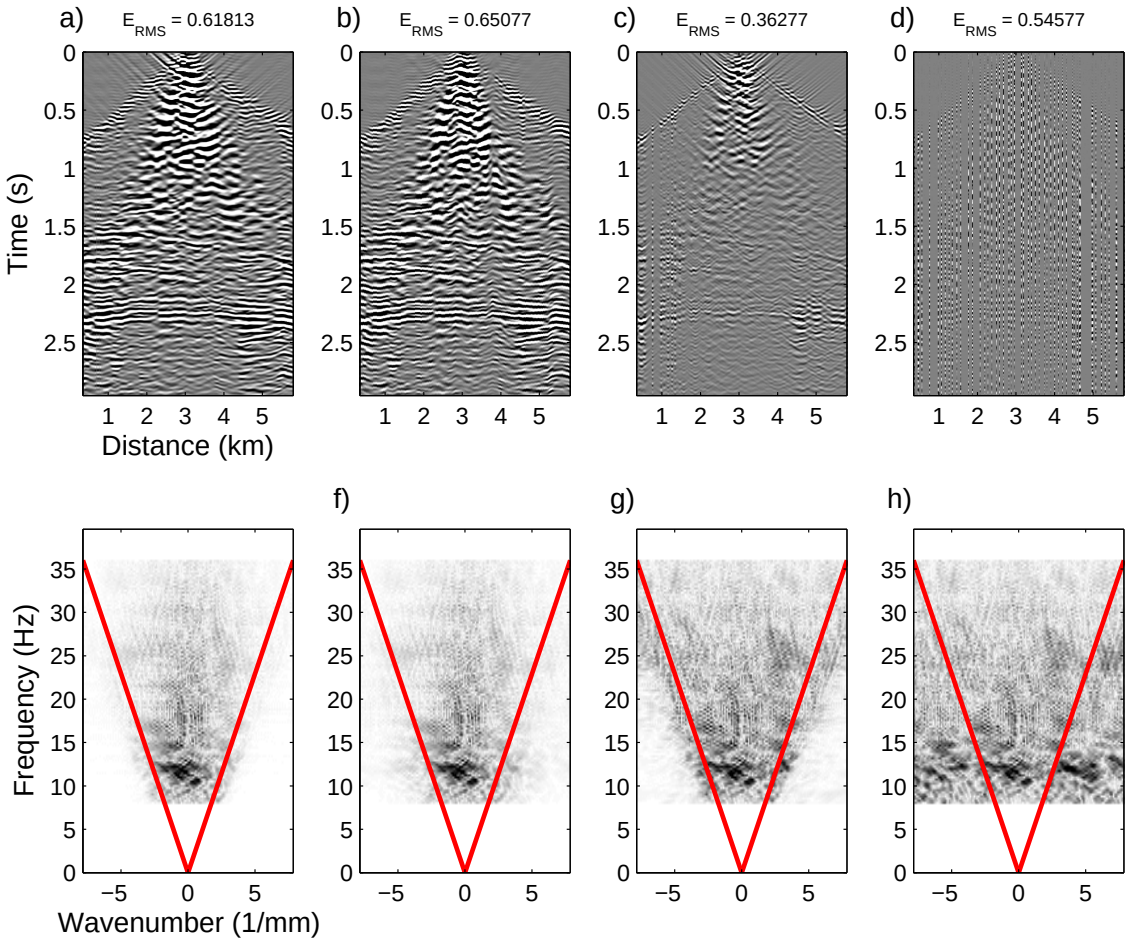

FIG. 21. Statics applied to the data shown in Figure 18c and b. a) Wave-equation statics by GPSPI applied to the data shown in Figure 18c. b) Conventional statics applied to Figure 18c. c) Wave-equation statics by GPSPI applied to Figure 18b. d) Conventional statics applied to Figure 18b. e) Spectrum of a. f) Spectrum of b. g) Spectrum of c. h) Spectrum of d. The evanescent boundary is indicated by red lines.